

1 **Trends of the high latitude mesosphere temperature and mesopause**
2 **revealed by SABER**

3 **Xiao Liu^{1,2}, Jiyao Xu^{2,3}, Jia Yue^{4,5}, Yangkun Liu^{1,2}, and Vania F. Andrioli^{2,6}**

4 ¹Institute of Electromagnetic Wave, School of Physics, Henan Normal University, Xinxiang,
5 453000, China

6 ²State Key Laboratory of Space Weather, National Space Science Center, Chinese Academy of
7 Sciences, Beijing, 100190, China

8 ³School of Astronomy and Space Science, University of the Chinese Academy of Science, Beijing,
9 100049, China

10 ⁴Catholic University of America, Washington, DC 20064, USA

11 ⁵NASA Goddard Space Flight Center, Greenbelt, MD, 20771, USA

12 ⁶Heliophysics, Planetary Science and Aeronomy Division, National Institute for Space Research
13 (INPE), Sao Jose dos Campos, Sao Paulo, Brazil

14

15 *Correspondence to: Jiyao Xu (xujy@nssc.ac.cn)*

16

17 **Key Points:**

- 18 • The mean temperature in the high latitude MLT region is obtained by binning the SABER
19 observations based on yaw cycles during 2002–2023
- 20 • In the high latitude MLT, the cooling trend is seasonal symmetric and reaches peak of ≥ 6
21 K/decade at highest latitudes around summer solstice
- 22 • The trends of mesopause temperature depend on latitudes but are mostly negative and have
23 larger magnitudes at highest latitude

24

25

26 **Abstract**

27 The temperature trend in the mesosphere and lower thermosphere (MLT) region can be
28 regarded as an indicator of climate change. Using temperature profiles measured by the Sounding of
29 the Atmosphere using Broadband Emission Radiometry (SABER) instrument during 2002–2023
30 and binning them based on yaw cycle, we get continuous dataset with wide local time coverage at
31 50°S–80°N or 80°S–50°N. The seasonal change of temperature, caused by the forward drift of
32 SABER yaw cycle, is removed by using the climatological temperature of MSIS2.0. The corrected
33 temperature without any waves is regarded as the mean temperature. At 50°S–50°N, the cooling
34 trends of the mean temperature are significant in the MLT region and are in agreement with
35 previous studies. The novel finding is that the cooling trends of ≥ 2 K/decade exhibit seasonal
36 symmetric and reach peaks of ≥ 6 K/decade at high latitudes around the summer solstice. Moreover,
37 there are warming trends of 1–2.5 K/decade at altitude range of 10^{-2} – 10^{-3} hPa, specifically at
38 latitudes higher than 55°N in October and December and at latitudes higher than 55°S in April and
39 August. The mesopause temperature (altitude) in the northern summer polar region is colder (lower)
40 than that in the southern counterpart by ~ 5 – 11 K (~ 1 km) over the past 22 years. The trends of the
41 mesopause temperature are dependent on latitudes and months. But they are negative at most
42 latitudes and reach larger magnitudes at high latitudes. These results indicate that the temperature in
43 the high latitude MLT region is more sensitive to dynamic changes.

44

45 **1 Introduction**

46 Observational and simulation studies have revealed that the global mean temperature trend is
47 cooling in the mesosphere and lower thermosphere (MLT) (Beig et al., 2003; Laštovička et al.,
48 2006; Yue et al., 2019b; Laštovička, 2023). The cooling trends observed in the MLT region are
49 mainly caused by the increasing anthropogenic greenhouse gases such as carbon dioxide. Moreover,
50 changes of the stratospheric ozone depletion and recovery, increasing mesospheric water vapor
51 concentration, solar and geomagnetic variations may also contribute to the long-term changes of
52 temperature in the MLT region (Laštovička, 2009; Yue et al., 2019a, 2015; Garcia et al., 2019;
53 Mlynczak et al., 2022; Zhang et al., 2023).

54 A recent review work by Laštovička (2023) summarized that temperature trends are generally
55 cooling but also depend on local times, heights, and geographic locations in the MLT region
56 (Venkat Ratnam et al., 2019; Das, 2021; She et al., 2019; Yuan et al., 2019; Ramesh et al., 2020).
57 These results were mostly derived from ground-based and satellite observations at low and middle
58 latitudes, while the simulations provided insights into the long-term trends from pole to pole. On the
59 other hand, the long-term trends in temperature at high latitudes have not been thoroughly examined
60 and well understood yet, due to scarce observations. Driven by the summer-to-winter meridional
61 circulation, the upwelling causes adiabatic cooling in the summer polar mesosphere, while the
62 downwelling causes adiabatic warming in the winter polar mesosphere (Dunkerton, 1978; Garcia
63 and Solomon, 1985). Thus, the high latitude temperature is more sensitive to the changes of
64 dynamics, wave and forcing, stratospheric wind etc. (Russell et al., 2009; Qian et al., 2017; Yu et
65 al., 2023).

66 The progress in studying long-term trends in the MLT region has been summarized and
67 reported by Laštovička and Jelínek (2019) and Laštovička (2023). Here we highlight some studies
68 related to the temperature trends at high latitudes. Using temperature measured by the Sounding of
69 the Atmosphere using Broadband Emission Radiometry (SABER) instrument and simulated by
70 Whole Atmosphere Community Climate Model version 4 (WACCM4), Garcia et al. (2019) showed
71 that the global mean SABER temperature (52°S – 52°N) had cooling trends of 0.4–0.5 K/decade
72 during 2002–2018 in the stratosphere and mesosphere. These magnitudes were smaller than those
73 simulated by WACCM4 (0.6–0.9 K/decade) but within 2 times of the standard deviation. Using
74 Leibniz Institute Middle Atmosphere Model (LIMA) under northern hemispheric conditions during
75 1871–2008, Lübken et al. (2018) showed that the cooling trend in the MLT region was 1.5 K/decade
76 during 1960–2008, and was 0.7 K/decade during 1871–2008 at 55 – 61°N on geometric heights.
77 However, the trend was neglectable on pressure heights. On pressure heights, the global mean
78 SABER temperature (55°S – 55°N) had cooling trends of 0.5 and 2.6 K/decade, respectively, at 10^{-3}
79 hPa (~ 92 km) and 10^{-4} hPa (~ 106 km) during 2002–2021 (Mlynczak et al., 2022). The results of

80 Lübken et al. (2018) and Mlynczak et al. (2022) illustrated that the cooling trends were larger over
81 recent decades on both geometric and pressure heights as compared to the beginning of
82 industrialization. To achieve a longer time series, Li et al. (2021) constructed a nearly 30-year
83 dataset at 45°S–45°N by merging the temperature measured by the Halogen Occultation Experiment
84 (HALOE) instrument during 1991–2005 and the SABER instrument during 2002–2019. They
85 showed that the cooling trend was significant and reached a peak of 1.2 K/decade at 60–70 km in
86 the Southern Hemisphere (SH) tropical and subtropical region. Moreover, the cooling trend in the
87 SH was larger than its counterpart in the Northern Hemisphere (NH).

88 At high latitudes, ground-based observations of OH nightglow rotational temperature revealed
89 a significant cooling trend of 1.2 ± 0.51 K/decade at Davis (68°S, 78°E) during 1995–2019 (French
90 et al., 2020). The OH rotational temperature around midnight exhibited a significant cooling trend
91 of $2.4 \text{ K} \pm 2.3$ /decade in summer and an insignificant cooling trend of 0.4 ± 2.2 K/decade in winter
92 at Moscow (57°N, 37°E) during 2000–2018 (Dalin et al., 2020). Using the ice layer parameters
93 simulated by the LIMA model and the Mesospheric Ice Microphysics And transport ice particle
94 model, Lübken et al. (2021) showed that the negative trend of noctilucent clouds altitudes (~83 km)
95 was primarily caused by the increasing CO₂ in the troposphere during 1871–2008 at 58°N, 69°N,
96 and 78°N. At these three latitudes, the cooling trends were of ~0.2 K/decade during 1871–1960 and
97 1.0 K/decade during 1960–2008. Near the latitude band of 64–70°N in June and 64–70°S in
98 December, Bailey et al. (2021) constructed two datasets by merging the temperature measured by
99 HALOE and SABER and by HALOE and SOFIE (Solar Occultation for Ice Experiment). They
100 showed that there were cooling trends of ~1–2 K/decade near 0.1–0.01 hPa (~68–80 km) and
101 warming trends of ~1 K/decade near 0.005 hPa (~85 km) at 64–70°N in June and 64–70°S in
102 December. Moreover, the WACCM-X simulation results by Qian et al. (2019) showed that the
103 temperature trends were mostly cooling in the MLT region. However, there were also warming at
104 ~80–95 km in the SH polar region from November to February (Fig. 3 of their paper). The
105 disagreement of these results at high latitudes might attribute to the different temporal spans and
106 local times, observations using different instruments, and different methods deriving the trends. It is
107 overarching to study the temperature trends at high latitudes using one coherent measurement over a
108 long period.

109 The SABER temperature profiles cover latitudes of 53°S–83°N in the north viewing
110 maneuvers and 83°S–53°N in the south viewing maneuvers since 2002. The operational SABER
111 temperature profile covers an altitude range of ~15–110 km. The precision and systematic error of
112 SABER temperature profile are height dependent. For a single temperature profile, its precisions are
113 summarized at <https://spdf.gsfc.nasa.gov/pub/data/timed/saber/> and are of 1.8 K at 80 km, 3.6 K at
114 90km, 6.7 K at 100 km, and 15.0 K at 110 km under the condition of vertical resolution of 2 km.

115 Moreover, for a single temperature profile, its systematic errors defined by one standard deviation
116 (corresponding to the confidence level of 68%) are of ~ 1.4 K at and below 80 km, 4.0 K at 90 km,
117 5.0 K at 100 km, and 25.0 K at 110 km for typical midlatitude condition (Remsberg et al., 2008;
118 Rezac et al., 2015; Dawkins et al., 2018). The systematic errors will be doubled if they are defined
119 by two times of standard deviation (corresponding to the confidence level of 95%). These data
120 exhibited remarkable stability over the last two decades following the correction of algorithm
121 instability (Mlynczak et al., 2020, 2022, 2023). Using the SABER temperature profiles during
122 2002–2019, Zhao et al. (2020) employed a 60-day moving window to obtain the mean temperature.
123 Their analysis revealed that the annual and global mean trend of mesopause temperature is cooling
124 with magnitude of 0.75 K/decade. Moreover, the cooling trend is significant in non-summer seasons
125 but insignificant in summer (May–August) at 60–80°N/S. It should be noted that, SABER yaw
126 cycle (YC) drifted forward about one month from 2002 to 2023 (see Fig. 1 below) due to changing
127 satellite orbit. This induces the local time (LT) coverage in a certain month differing from year to
128 year at high latitudes if the window is set to be constantly 60-day.

129 Here we focus on the trend of the mean temperature without any atmospheric waves (i.e.,
130 gravity waves, tides and planetary waves). Calculating zonal mean can remove gravity waves,
131 nonmigrating tides and long-period planetary waves. However, migrating tides depend on LT and
132 are strong in the MLT region. They cannot be simply removed by calculating zonal mean. In this
133 work, we bin the data based on YC, which covers an interval of 54–64 days (see Fig. 1 below) and
134 provides almost full local time coverage (except the 1–3 hours around noon). Thus, the mean
135 temperature can be accurately determined by removing the migrating tides at 53°S–83°N or 83°S–
136 53°N using harmonic fitting. Each YC at every year covers varying ranges of dates. This results in
137 the aliasing of the seasonal variation of temperature into the mean temperature of each YC. This
138 issue can be resolved as below. We use the temperature of the recently released whole-atmosphere
139 empirical model MSIS2.0 (Emmert et al., 2021) as a reference for the seasonal variation. This
140 seasonal variation (more than 10 K as seen in Fig. 2b) embedded in YC drift is removed from the
141 mean temperature of each YC. Thus, using the advantages of SABER measurements at high
142 latitudes and binning the data based on YC, we focus on the long-term trends of the mean
143 temperature and the mesopause in the high latitude MLT region.

144 **2 Method of calculating mean temperature and trend**

145 The mean temperature (\bar{T}_{bk}) excludes gravity wave, tides and planetary waves. Moreover,
146 compared to the magnitudes of \bar{T}_{bk} , its trend is a small value and should be determined with extra
147 caution. The method of calculating \bar{T}_{bk} is based on a YC window. This ensures a good LT coverage
148 at high latitudes. Compared to the fixed 60-day window, the advantage and necessity of the YC

149 window are described below.

150 The YC window is defined as the temporal interval during which the SABER measurements
 151 are in the northward or southward viewing maneuver. Figure 1 shows the beginning date and
 152 temporal span of each YC. We see that there are about six YCs in each year, being named as YC1–
 153 YC6. The temporal spans of YCs are 54–64 days. This ensures that the LT coverage of SABER
 154 samplings is more than 18 hours at high latitudes. Therefore, migrating tides can be removed
 155 efficiently through harmonic fitting. In contrast, the LT coverage in a fixed 60-day window is
 156 different from year to year at high latitudes. This is because the temporal span of each YC drifted
 157 forward about one month from 2002 to 2023 (Fig. 1). For the case of the fixed 60-day window and
 158 at 70°N and in March (spanning from 14th February to 14th April with a center on 15th March), the
 159 sampling hours distributed at 0–2, 5–11, and 21–24 LT and had a coverage of only 14 hours in
 160 2005. However, the sampling hours in 2022 distributed at 0–10 and 13–24 LT and had a coverage of
 161 22 hours. The year-to-year variations of LT distribution and coverage might induce uncertainties
 162 and biases into \bar{T}_{bk} . Thus, the YC dependent window is necessary to obtain a wide LT coverage.

163

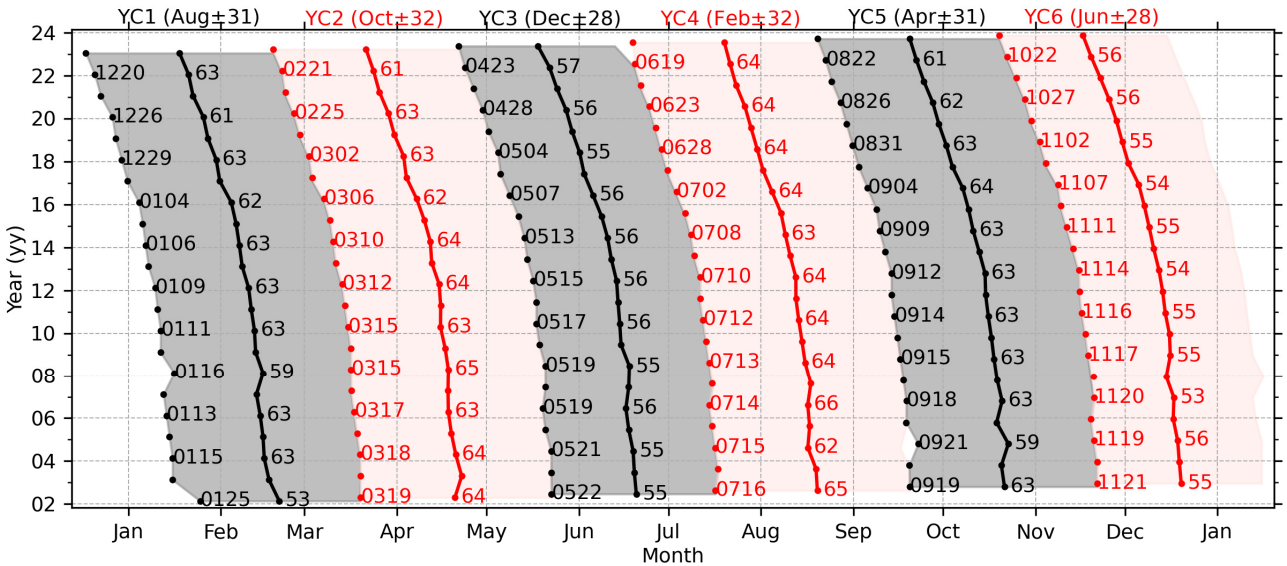


Figure 1. The temporal span of each YC from 2002 to 2023. The gray (red) region indicates the north (south) viewing maneuver. The beginning date (format of “mmdd”, “mm” and “dd” mean the month and the day of month, respectively) and temporal span (unit of days) of each yaw are labeled on the right of beginning (dot) and center date (dot-line), respectively. The six YCs and their center date in 2003 and half spans and are labeled as YC1–YC6 on the top.

164

165 We note that the forward drift of YC raises an issue that each YC at every year covers varying
 166 ranges of date. This aliases seasonal variation of temperature into \bar{T}_{bk} and should be removed to get
 167 a corrected mean temperature (\bar{T}_{bcrt}). The detailed procedure of the calculating \bar{T}_{bcrt} and its trend is

168 presented in Sec. 2.1–2.3. The procedure of calculating mesopause temperature and height is
169 presented in Sec. 2.4.

170 2.1 Removing waves from SABER temperature

171 In each YC, the background temperature is calculated at three steps. Firstly, at each latitude
172 band and pressure level, the daily zonal mean temperature (\bar{T}_d) is calculated by averaging the
173 temperature profiles at ascending and the descending nodes, respectively. This largely removes the
174 gravity waves, non-migrating tides, and long-period planetary waves. Here each latitude band has a
175 width of 10° with centers offset by 5° from 80°S to 80°N . Secondly, linear regression is performed
176 on \bar{T}_d at each node and is formulated as,

$$177 \quad \bar{T}_d = \bar{T}_{d0} + kt_{UT} + \bar{T}_{res}. \quad (1)$$

178 Here, \bar{T}_{d0} is the mean temperature in each YC. t_{UT} is the universal time with a unit of day, k
179 represents the linear variation of \bar{T}_d in each YC. After removing \bar{T}_{d0} and the linear variation (kt_{UT})
180 from \bar{T}_d , we get a residual temperature \bar{T}_{res} of each YC. Thirdly, tidal fitting is performed on \bar{T}_{res} of
181 both nodes and is formulated as,

$$182 \quad \bar{T}_{res} = \bar{T}_{bk} + \sum_{n=1}^3 a_n \cos(n\omega t_{LT} - \varphi_n). \quad (2)$$

183 Here, $\omega = 2\pi/24$ is the rotation frequency of Earth with a unit of rad/hour, t_{LT} is the local time
184 with a unit of hour, a_n and φ_n are, respectively, the amplitudes and phases of migrating diurnal
185 ($n = 1$), semidiurnal ($n = 2$) and terdiurnal ($n = 3$). Now, \bar{T}_{bk} excludes atmospheric waves and is
186 regarded as the mean temperature.

187 2.2 Removing seasonal variations from the mean temperature

188 Figure 1 shows that the center date of each YC shifts forward about one month from 2002 to
189 2023. This forward drift induces the seasonal variation of temperature into \bar{T}_{bk} . This could further
190 alias the long-term trend calculated from \bar{T}_{bk} and can be removed with the help of MSIS2.0. This is
191 because MSIS2.0 has assimilated the SABER temperature profiles during 2002–2016. The
192 climatological temperature of MSIS2.0 coincides with that of SABER within the uncertainties of \sim
193 3 K in the MLT region (Emmert et al., 2021). The detailed procedure of removing seasonal
194 variations is described below.

195 Firstly, we calculate the mean temperature of MSIS2.0. The temperature profiles (at 15
196 longitudes and 24 LTs each day) are calculated from MSIS2.0 under the conditions of lower solar
197 activity ($F_{10.7} = 50$ SFU) and geomagnetic quiet time ($ap = 4$ nT) throughout one calendar year.
198 Such that solar and geomagnetic activities do not influence the seasonal variation and trend of the
199 mean temperature. Then the daily zonal mean is performed on the temperature profiles of each day.
200 This removes tides and long-period planetary waves. The daily zonal mean temperature in each YC
201 is averaged to get the mean temperature (\bar{T}_{MSIS}^{year} , the superscript means the YC in that year). Figures

202 2(a1) and (a2) show the \bar{T}_{MSIS}^{year} at 70°N in YC3 and 70°S in YC6 during 2002–2023, respectively.

203 Secondly, we calculate the seasonal variations of each YC. The seasonal variations ($\Delta\bar{T}_{MSIS}^{year}$)
 204 caused by the forward drift of each YC in different years are quantified by the difference between
 205 \bar{T}_{MSIS}^{year} of that year and the reference year (i.e., \bar{T}_{MSIS}^{2002}). For example, the difference between 2003
 206 and 2002 is calculated as $\Delta\bar{T}_{MSIS}^{2003} = \bar{T}_{MSIS}^{2003} - \bar{T}_{MSIS}^{2002}$. More specifically, since \bar{T}_{MSIS}^{year} does not include
 207 the year-to-year variations of temperature but depends on the temporal span of YC only, $\Delta\bar{T}_{MSIS}^{2003}$ in
 208 YC3 represents the seasonal variation from 20th to 19th June. Figures 3(b1) and (b2) show $\Delta\bar{T}_{MSIS}^{year}$ at
 209 70°N in YC3 and 70°S in YC6 during 2002–2023, respectively. It is evident that the forward drift of
 210 YC induces temperature variations of ± 20 K at 70°N/S from 2002 to 2023, and should be removed
 211 before we determine the long-term trends in SABER temperature.

212

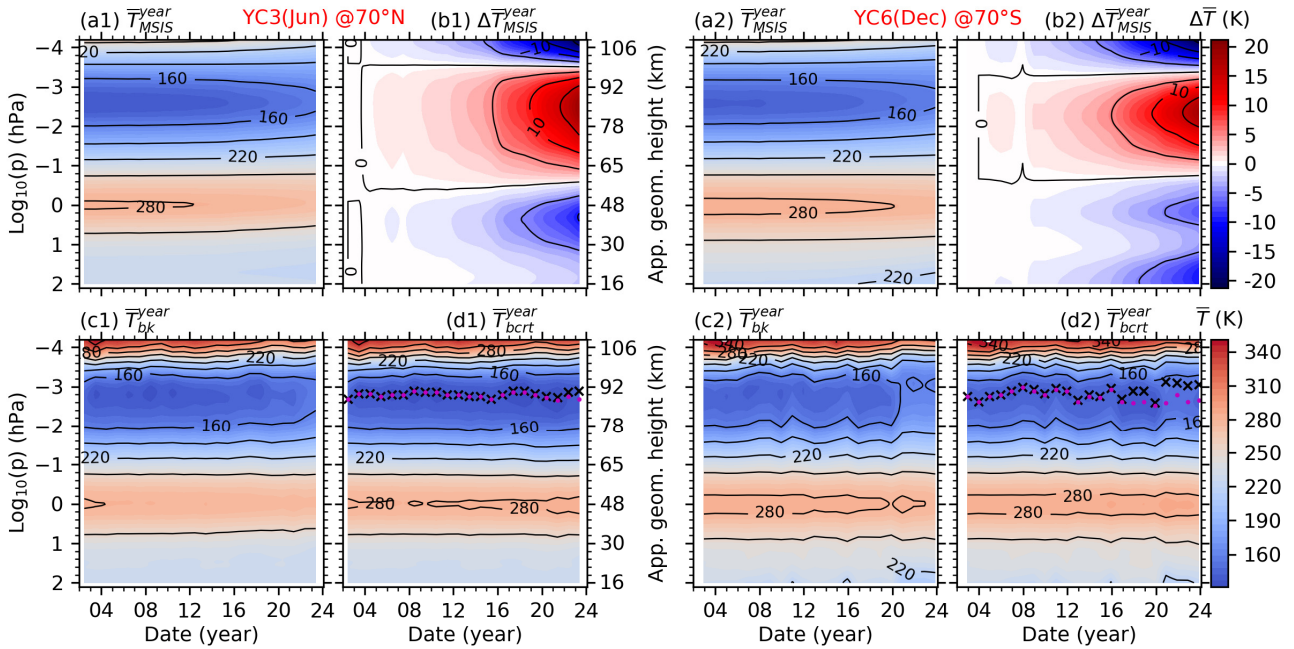


Figure 2. The date-height distributions of the mean temperature calculated from NRLMSIS 2.0 (\bar{T}_{MSIS}^{year}) and SABER (\bar{T}_{bk}^{year}) at 70°N in YC3 (left two columns) and 70°S in YC6 (right two columns). \bar{T}_{MSIS}^{year} is used as a reference to calculate the seasonal variation ($\Delta\bar{T}_{MSIS}^{year}$) caused by the forward drift of YC from 2002 to 2023. Then, the corrected mean temperature (\bar{T}_{bcrt}^{year}) is calculated by removing $\Delta\bar{T}_{MSIS}^{year}$ from \bar{T}_{bk}^{year} . The mesopause altitudes calculated from \bar{T}_{bk}^{year} and \bar{T}_{bcrt}^{year} are plotted as black cross and red dots, respectively. The plots of \bar{T}_{MSIS}^{year} , \bar{T}_{bk}^{year} , and \bar{T}_{bcrt}^{year} have the same colorbar of \bar{T} . The plot of $\Delta\bar{T}_{MSIS}^{year}$ has the colorbar of $\Delta\bar{T}$. Same scales in y-axis are used in all panels. The approximate geometric height is label on the right of the second column.

213

214 Finally, we correct the mean temperature. The corrected mean temperature (\bar{T}_{bcrt}^{year} , shown in
 215 Figs. 3d1 and d2) is obtained by removing $\Delta\bar{T}_{MSIS}^{year}$ from \bar{T}_{bk}^{year} . This removes the seasonal variation

216 caused by the forward drift of YC from 2002 to 2023. Moreover, \bar{T}_{bcrt}^{year} retains the long-term trend
 217 of the mean temperature. We note that, after removing $\Delta\bar{T}_{MSIS}^{year}$, \bar{T}_{bcrt}^{year} covered by each YC can be
 218 represented by its center date and half span in the reference year (Tab. 1). Table 1 also lists the
 219 approximate season related to each YC.

220

221 **Table 1.** The date range of each YC and its corresponding season in the reference year of 2003

YCs	YC1	YC2	YC3	YC4	YC5	YC6
Date range	20/Feb±31	20/Apr±32	20/Jun±28	19/Aug±32	13/Oct±31	10/Dec±28
Season	later winter	later spring	summer	early autumn	later autumn	winter

222

223 2.3 Determining the long-term trend of the mean temperature

224 To calculate accurate trends in the MLT region, multi-year variations should be removed
 225 properly. The multi-year variations of temperature in the MLT region could be the solar cycle with a
 226 period of about 11 years (Beig et al., 2008; Tapping, 2013; Forbes et al., 2014; Gan et al., 2017;
 227 Qian et al., 2019), and the influences from below, such as the El Niño-Southern Oscillation (ENSO)
 228 with varying cycles of around 2–7 years (Domeisen et al., 2019; Li et al., 2013, 2016; Randel et al.,
 229 2009). The solar cycle can be represented by the solar radiation flux at 10.7 cm (i.e., $F_{10.7}$ with unit
 230 of SFU= $10^{-22}\text{Wm}^{-2}\text{Hz}^{-1}$) (Tapping, 2013). ENSO is represented by multivariate ENSO index (MEI)
 231 (Domeisen et al., 2019). The multiple linear regression (MLR) method is effective to separate the
 232 long-term trend in temperature from the variations caused by solar cycle, ENSO and QBO. The
 233 MLR equation is formulated as,

$$234 \quad Y(t) = c_0 + c_1 t + c_2 F_{10.7}(t) + c_3 \text{ENSO}(t) + \varepsilon(t). \quad (3)$$

235 Here, Y represents the mean temperature at year t from 2002 to 2023. c_0 represents a mean state of
 236 Y . c_1 is the long-term trend of Y . c_2 , c_3 represent the contributions from solar cycle and ENSO,
 237 respectively. The terms of $F_{10.7}$ and ENSO are included in Eq. (3) for the purpose of determining
 238 long-term trend correctly but are not considered further in this work. Here we note that both the
 239 trends (linear variations) and quasi-periodical variations represent the natural variations in the
 240 predictors. These natural variations might influence the trends and variations of temperature. Thus,
 241 MLR is applied to characterize the contributions from the natural variations of predictors, and then
 242 the resulted trends of temperature exclude the trends inhibited in the predictors. This is the trend
 243 studied in this work. Otherwise, if these predictors are de-trended, their residuals are used in the
 244 MLR. The resulted trends of temperature may include the trends inhibited in predictors.

245 The statistical significances of the regression coefficients are measured by the student-t test
 246 and the variance-covariance matrix of Eq. (3). Specifically, in Eq. (3), the sampling points are 22,

247 and the predictor variables are 4. This results in the degree of freedom of 19. Consequently, the
248 critical value is ~ 2.0 based on the student-t test at confidence level of 95% (Kutner et al., 2005).
249 This signifies that, with reference to the 95% confidence level, the magnitude of the regression
250 coefficient should be at least 2.1 times greater than the standard deviation.

251 **2.4 Determining the mesopause of each yaw cycle**

252 The mesopause temperature (\bar{T}_{msp}) is defined as the minimum of the mean temperature. The
253 pressure level where the minimum temperature occurs is defined as the mesopause altitude (z_{msp}).
254 Figures 2(d1) and (d2) show the mesopause altitudes calculated from \bar{T}_{bk}^{year} (black cross) and \bar{T}_{bcrt}^{year}
255 (red dot), respectively. We see that the mesopause altitudes calculated from \bar{T}_{bk}^{year} and \bar{T}_{bcrt}^{year} are
256 nearly identical in the first several years but exhibit discrepancies over the later several years. This
257 implies that the seasonal variation caused by the forward drift of YC affects the mesopause altitudes
258 to some extent. Moreover, the mesopause altitudes exhibit larger variabilities in the southern
259 summer polar region (YC6) than that in the northern summer polar region (YC3). Figure 3 shows
260 the date-latitude distributions of the mesopause temperature (\bar{T}_{msp}) and altitude (z_{msp}) calculated
261 from \bar{T}_{bcrt}^{year} . We note that z_{msp} is defined on pressure level initially (Fig. 2d). To compare with
262 previous studies, z_{msp} is interpolated onto the geometric heights in Fig. 3.

263 Previous SABER studies often discarded high latitudes possibly due to insufficient LT
264 coverage that induces uncertainties in the mean temperature estimation. A major advantage of
265 binning the SABER temperature based on YC is that an accurate mean temperature can be obtained.
266 Such that the latitude variations of \bar{T}_{msp} and z_{msp} at high latitudes can be thoroughly studied.
267 Firstly, we focus on the YCs in northern summer and winter (i.e., YC3 and YC6) because the
268 summer mesopause at high latitudes is more sensitive to the summer-to-winter circulation
269 (Dunkerton, 1978; Qian et al., 2017). In YC3 (YC6), \bar{T}_{msp} and z_{msp} decrease from 50°S to 80°N
270 (from 50°N to 80°S) in general. We note that \bar{T}_{msp} has local minima around the Equator throughout
271 the 22 years in YC3 and YC6 and is the coldest at the highest latitudes of the summer hemisphere.
272 z_{msp} is the lowest at 40–60°N/S throughout the 22 years. Besides the latitude variations, \bar{T}_{msp} and
273 z_{msp} also exhibit multi-year variations. For example, \bar{T}_{msp} is colder around the Equator during the
274 solar minima (i.e., 2007–2008, 2019–2021) in YC3 and YC6. In YC6, the lower z_{msp} at the
275 southern higher latitudes might be related to the warm phase of ENSO during 2002–2005 and
276 2016–2019.

277

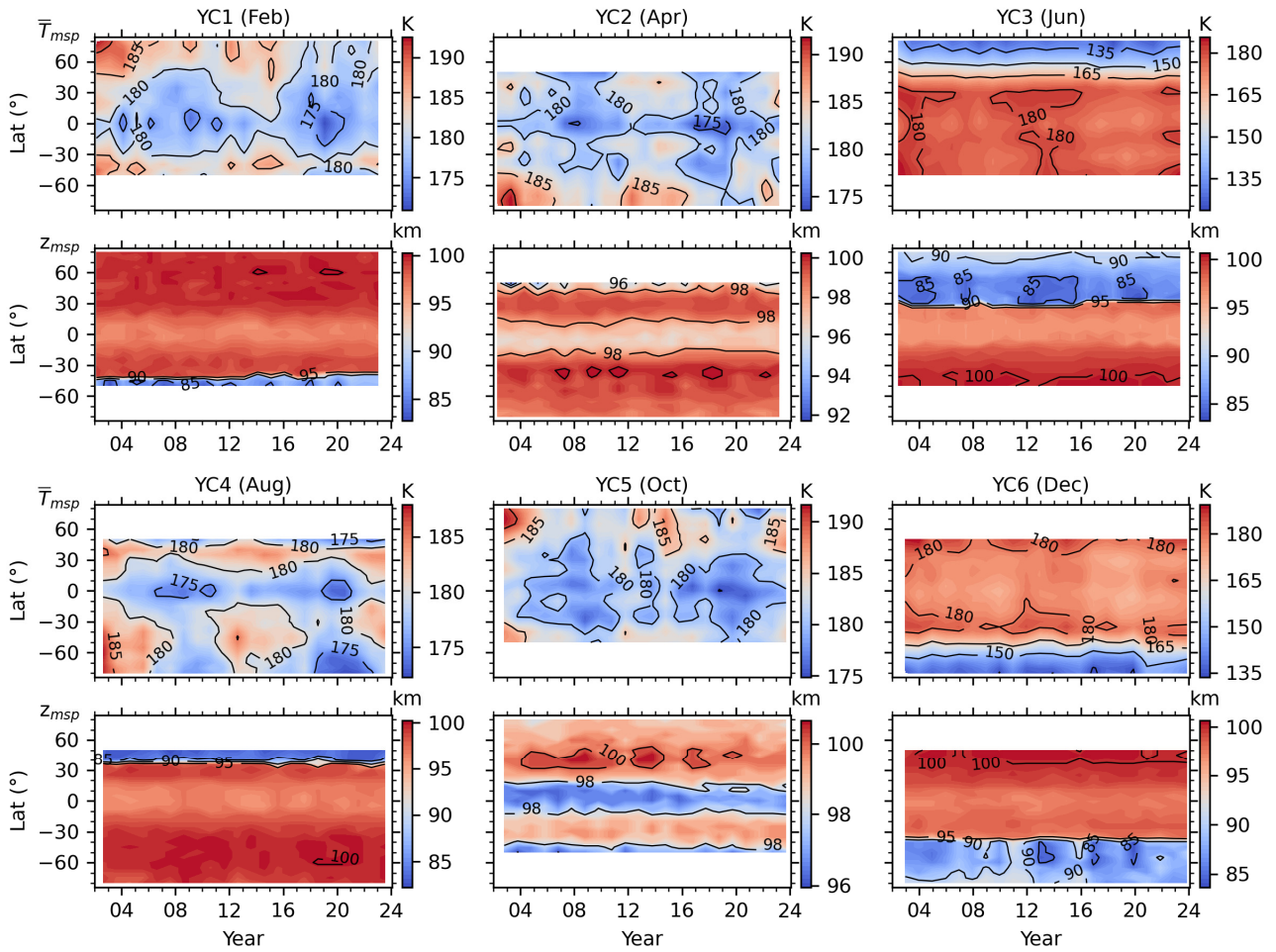


Figure 3. The date-latitude distributions of the mesopause temperature (\bar{T}_{msp} , the first and third rows) and altitude (z_{msp} , the second and fourth rows) calculated from \bar{T}_{bcrt}^{year} of each YC from 2002 to 2023. Here z_{msp} is interpolated from pressure level to geometric height.

278

279 In YC2 and YC5, the latitude variations of \bar{T}_{msp} and z_{msp} are almost hemispheric symmetry.
 280 \bar{T}_{msp} is the coldest around the Equator and the warmest at the highest latitudes. z_{msp} is the lowest at
 281 lower latitudes and the highest at the highest latitudes. In YC1, \bar{T}_{msp} and z_{msp} share the similar
 282 latitude variations in winter (YC6). The difference is that \bar{T}_{msp} is warmer in YC1 than that in YC6.
 283 z_{msp} is higher in YC1 than that in YC6. In YC4, \bar{T}_{msp} and z_{msp} share the similar latitude variations
 284 in summer (YC3). The difference is that \bar{T}_{msp} is warmer in YC4 than that in YC3. z_{msp} is higher in
 285 YC4 than that in YC3. In YC1–2 and YC4–5, multi-year variations of \bar{T}_{msp} exhibit clear solar cycle
 286 dependence. At lower latitudes, \bar{T}_{msp} are colder during the solar minima (i.e., 2006–2010, 2017–
 287 2021). At high latitudes, \bar{T}_{msp} are warmer during the solar maxima (i.e., 2002–2005, 2012–2014,
 288 and after 2021). However, it looks like that the multi-year variations of z_{msp} are not as obvious as
 289 those of \bar{T}_{msp} . These multi-year variations are considered in Eq. (3) to separate the long-term trend
 290 in \bar{T}_{msp} correctly but are not considered further in this work.

291 3 Trends of temperature in the MLT region and mesopause

292 3.1 Trends of temperature in the MLT region

293 Trends of the corrected mean temperature and their significances of each YC are shown in Fig.
294 4. These trends are generally larger at high latitudes than those at lower latitudes within the six YCs.
295 Moreover, the trends show both hemispheric symmetry and asymmetry approximately in the high
296 latitude MLT region.
297

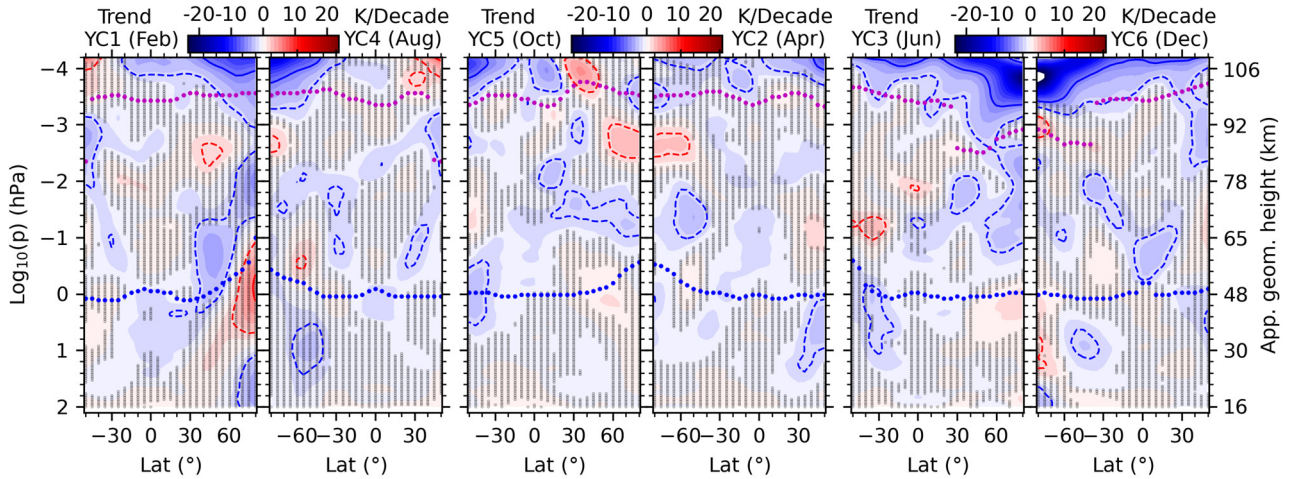


Figure 4. Trends of the corrected mean temperature in the six YCs. The solid and dashed contour lines indicate ± 6 and ± 2 K/decade, respectively. The purple and blue dots indicate the heights of the mesopause and stratopause, respectively. The regions marked by shaded points indicate that trends are not significant with reference to the 95% the confidence level. The approximate geometric height is label on the last panel.

298

299 First, we describe the hemispheric symmetry in the trends. In YC1 and YC4 and above 10^{-3}
300 hPa, the cooling trends are ≥ 2 K/decade at latitudes higher than 40°N (YC1) and 40°S (YC4),
301 respectively. Around 10^{-4} hPa, the cooling trends reach their peaks of ≥ 6 K/decade. In addition,
302 there are also warming trends of ≥ 2 K/decade at latitudes higher than 30°S (YC1) and 30°N (YC4),
303 respectively. Above mesopause, there are cooling trends of ≥ 2 K/decade observed within the latitude
304 range of $20\text{--}50^\circ\text{S}$ for YC5 and $20\text{--}50^\circ\text{S}$ for YC2. Additionally, in the region just below 10^{-3} hPa,
305 there are warming trends of ≥ 2 K/decade at latitudes of $50\text{--}80^\circ\text{N}$ for YC5 and $50\text{--}80^\circ\text{S}$ for YC2. In
306 YC3 and YC6, the cooling trends of ≥ 2 K/decade shift upward from the mesopause at 80°N (YC3)
307 and 80°S (YC6) to 10^{-4} hPa at 50°S (YC3) and 50°N (YC6). There are also cooling trends of ≥ 6
308 K/decade at high latitudes of summer hemisphere. Meanwhile, the coldest trends are ≥ 10 K/decade
309 just below 10^{-4} hPa and at 80°N/S . Although the cooling trends in the MLT region have been
310 reported extensively at lower and middle latitudes (Beig et al., 2003; Laštovička, 2023), the extreme
311 cooling trends at high latitudes and above the summer mesopause have not been reported yet. We

312 note that the systematic error in the SABER operational processing is unknown. Its impacts on the
313 credibility of the trends derived here will be discussed in Sec.4.

314 Next, we describe the hemispheric asymmetry in the trends. In YC1 and YC4, the cooling
315 trends of ≥ 2 K/decade in YC1 extend to a wider latitude range (20°N – 80°S) than those in YC4
316 (30°S – 80°S) above 10^{-3} hPa. The insignificant warming trends of ≥ 2 K/decade can be seen in the
317 stratosphere at latitudes higher than 60°N in YC1 but at 45 – 60°S in YC4. In YC5 and YC2, the
318 cooling trends of ≥ 2 K/decade can be seen around the stratopause at 30 – 50°S (YC5) but below the
319 stratopause at 30 – 50°N (YC2). In YC3 and YC6, the significant warming trends of ≥ 2 K/decade in
320 YC6 are stronger than those in YC3 around 0.1 hPa. In addition, the warming trends near the
321 summer mesopause are significant in YC6 but insignificant in YC3. The simulation results in Qian
322 et al. (2019) also demonstrated warming trends in the southern summer MLT region. Specifically,
323 they showed significant warming trends below ~ 95 km and cooling trends above ~ 95 km at
324 latitudes exceeding 45°S between November and February. In contrast, there were insignificant or
325 warming trends at latitudes exceeding 45°N during June and July. Qian et al. (2019) attributed the
326 warming trend in the summer mesosphere to the changing meridional circulation.

327 **3.2 Structure and trends of the mesopause**

328 Taking advantages of the continuous measurements over a long-term (22 years or equivalently
329 two solar cycles), and YC binning at 50°S – 80°N or 80°S – 50°N , the robust mean states of the
330 mesopause temperature (\bar{T}_{msp}) and height (z_{msp}), as well as their trends and responses of \bar{T}_{msp} to
331 solar cycle, ENSO, QBO are quantified using MLR. Here we focus on the mean states and trends of
332 the mesopause temperature and altitude.

333 Figures 5(a) and 5(b) show the mean \bar{T}_{msp} and z_{msp} over 22 years of the six YCs. In YC1–2
334 and YC4–5, the mean \bar{T}_{msp} is in the range of 172–183 K but is warmer at latitudes higher than 40°N
335 (YC1) and 40°S (YC2) those in the counterparts of YC4 and YC5. The mean z_{msp} is mainly in the
336 range of ~ 96 – 102 km but is higher than ~ 85 km at 40 – 50°N (YC1) and 40 – 50°N (YC4). In YC3,
337 the mean \bar{T}_{msp} decreases sharply with latitudes from ~ 180 K at 30°N to ~ 125 K at 80°N . The mean
338 z_{msp} in YC3 reaches a minimum of ~ 85 km at 60°N . In YC6, the mean \bar{T}_{msp} decreases sharply with
339 latitudes from ~ 180 K at 35°S to ~ 135 K at 80°S . The mean z_{msp} in YC6 reaches a minimum of
340 ~ 86 km at $\sim 50^{\circ}\text{S}$. The mean \bar{T}_{msp} (z_{msp}) in the northern summer polar region is colder (lower) than
341 that in the southern counterpart by ~ 5 – 11 K (~ 1 km). The hemispheric asymmetries of the summer
342 mesopause temperature and altitude coincide with Xu et al. (2007), who used the SABER
343 temperature data during 2002–2006 and showed that the mean \bar{T}_{msp} in the summer polar region of
344 the NH is ~ 5 – 10 K colder than its counterpart in the SH. A recent study by Wang et al. (2022), who
345 used the SABER temperature data during 2002–2020, showed that the mean \bar{T}_{msp} in the summer

346 polar region of the NH is ~ 10 K colder than its counterpart in the SH. Moreover, the transition
 347 latitudes of the mean \bar{T}_{msp} (z_{msp}) from higher temperature (height) are 30°N in YC3 and 40°S in
 348 YC6. This coincides well with those reported by Xu et al. (2007) and Wang et al. (2022). These
 349 hemispheric asymmetries of the mean \bar{T}_{msp} and z_{msp} , and the transition latitudes could be caused
 350 by the hemispheric asymmetry of solar radiation and gravity wave forcing (Xu et al., 2007).
 351

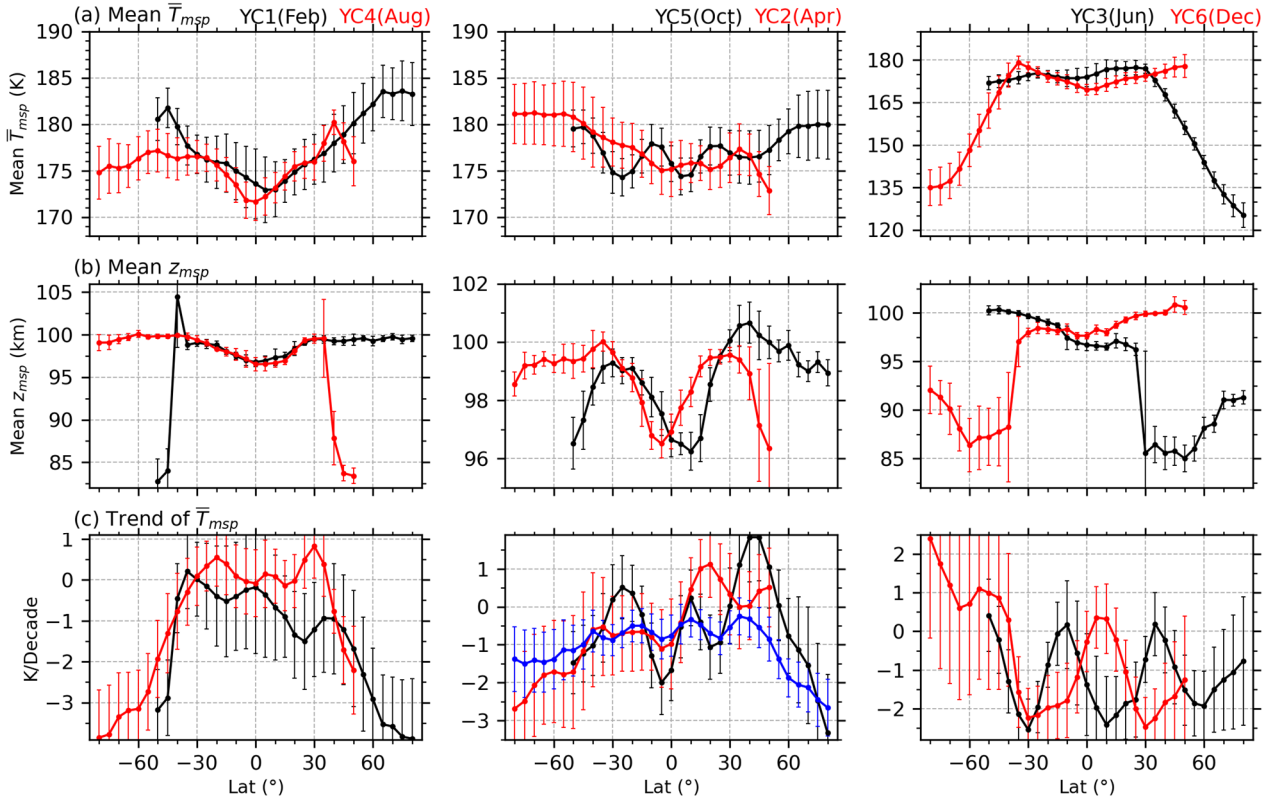


Figure 5. Latitude variations of the means of the mesopause temperature (\bar{T}_{msp} , a) and altitude (z_{msp} , b) and the trends of \bar{T}_{msp} (c) of the six YCs during 2002–2023. The error bar of each YC indicates 2.1 times standard deviation (i.e., at 95% confidence level according to the student-t test). The all-YC mean trend of mesopause temperature is shown as a blue line in the middle panel of (c).

352

353 Figure 5c shows that trends of \bar{T}_{msp} in YC1 and YC4 are extreme cooling (≥ 2 K/decade) at
 354 latitudes higher than 55°N/S . While at 40°S – 40°N , trends of \bar{T}_{msp} in YC1 are cooling with
 355 magnitudes of ~ 0 – 2 K/decade but are warming in YC4 with magnitudes of ~ 0 – 1 K/decade. In YC2
 356 and YC5, trends of \bar{T}_{msp} are either cooling or warming, depending on the specific latitudes and
 357 months being considered. At southern latitudes, trends of \bar{T}_{msp} are cooling with magnitudes of ≥ 1
 358 K/decade in YC2. Trends of \bar{T}_{msp} in YC5 change sharply from 2.0 K/decade at 45°N to -3
 359 K/decade at 80°N . In YC3 and YC6, trends of \bar{T}_{msp} are mainly cooling except the insignificant
 360 warming trends in YC6 and at latitudes higher than 40°S . Although trends of \bar{T}_{msp} are warming at

361 some latitudes of certain YC, the all-YC mean trends of \bar{T}_{msp} (blue line in Fig. 5c) are cooling with
362 magnitudes of 0.3–1 K/decade at 50°S–50°N. At latitudes higher than 55°S, the insignificant
363 cooling trends are ≤ 1.5 K/decade. In contrast, at latitudes higher than 55°N, the significant cooling
364 trends are ≥ 1.5 K/decade.

365 4 Discussions

366 The trends derived here may be influenced by the unknown systematic errors in the SABER
367 operational processing. The main causes of systematic errors are the lack of accurate knowledge of
368 the uncertainties in key parameters (mixing ratios of atomic oxygen (O) and carbon dioxide (CO₂))
369 and the nature of non-LTE (local thermodynamic equilibrium) in the SABER temperature retrieval.
370 The O mixing ratio provided to the SABER operational processing is from NRLMSISE-00 (Picone
371 et al., 2002). Below 100 km, no atmospheric observations of O are incorporated. Thus, the
372 uncertainty of O influences the uncertainties of temperature at ~ 75 –110 km, in particular at 100–
373 110 km. The CO₂ mixing ratio provided to the SABER operational processing is the monthly
374 average value from WACCM model (Dawkins et al., 2018; Mlynczak et al., 2023). Thus, there is no
375 local time variation in CO₂ used in the operational SABER operational processing. The larger
376 vertical diffusion used in WACCM4 as compared to WACCM3 led to 15% uncertainty in CO₂ at
377 110 km. Mlynczak et al. (2023) showed that 15% uncertainty in CO₂ at 110 km an 8 K error in the
378 global mean (55°S–55°N) temperature. Moreover, the lack of correct trends and their coupling with
379 dynamical adjustments in O and CO₂ may also be sources of the systematic errors in SABER
380 temperature at high altitudes. At high altitudes and latitudes, non-LTE radiative transfer in CO₂
381 couples the vibrational temperatures at all altitudes due to the exchange of radiation among all
382 layers. Thus, any uncertainties in O or CO₂ at one layer will affect the temperature at all altitudes.
383 These uncertainties are systematic errors and cannot be reduced by averaging many profiles. Thus,
384 the trends derived here should be discussed rigorously based on the systematic errors of a single
385 temperature profile.

386 As reported at SABER web (<https://spdf.gsfc.nasa.gov/pub/data/timed/saber/>), one standard
387 deviation (corresponding to the confidence level of 68%) of the systematic error for a single
388 temperature profile is of ~ 1.4 K at and below 80 km, 4.0 K at 90 km, 5.0 K at 100 km, and 25.0 K
389 at 110 km for typical midlatitude condition. These errors may be larger at high latitudes. A rigorous
390 systematic error analysis is performed by assuming a negative systematic error (-E) in 2002 and a
391 positive systematic error (+E) in 2023. The difference of the two numbers over the 22 years is the
392 largest uncertainty caused by the systematic error (i.e., $2E/22 \approx 0.9E$ K/decade) and is named as
393 systematic trend uncertainty. Then, the number E is replaced by the systematic error reported at
394 SABER web. Such that one can get a systematic trend uncertainty for a given systematic error. We

395 note that the systematic trend uncertainty of 0.9E K/decade is the largest uncertainty caused by the
396 systematic error and is the worst case among all the combinations of systematic errors in different
397 years.

398 Based on the systematic error defined by one standard deviation at SABER web, the
399 systematic trend uncertainty during 2002–2023 caused by systematic errors at 110 km
400 ($\sim\log_{10}(6.3\times 10^{-5}\text{ hPa}) = -4.2$) can be estimated as 50 K / 22 years $\approx \pm 22.7$ K/decade. In a same
401 manner, the systematic trend uncertainties are of 4.5 K/decade at 100 km ($\sim\log_{10}(2.8\times 10^{-4}\text{ hPa}) = -$
402 3.6), 3.6 K/decade at 90 km ($\sim\log_{10}(1.4\times 10^{-3}\text{ hPa}) = -2.9$), and 1.3 K/decade at and below 80 km
403 ($\sim\log_{10}(6.6\times 10^{-3}\text{ hPa}) = -2.2$). We note that the systematic trend uncertainty will be doubled if the
404 systematic error is defined by two times of standard deviation (corresponding to the confidence
405 level of 95%). In the following discussions, we will compare the trends derived here with previous
406 observations and the systematic trend uncertainty calculated from the systematic error defined by
407 one standard deviation. If the derived trend is larger than the systematic trend uncertainty, the trend
408 is reliable. Otherwise, the trend is questionable.

409 The temporal interval of data may also influence the long-term trend (Laštovička and Jelínek,
410 2019). Using the nocturnal temperature in the MLT region measured by lidars around 41°N and
411 42°N over the period of 1990–2017, She et al. (2019) demonstrated that the cooling trends are
412 ~ 2.0 – 4.5 K/decade over only one solar cycle and are ~ 2.0 – 2.5 K/decade if the data length is longer
413 than two solar cycles. Using the SABER temperature profiles during 2002–2019, Zhao et al. (2020)
414 showed that the significant trends of \bar{T}_{msp} and their responses to solar cycle can be obtained at
415 50°S–50°N over longer than one solar cycle. Both She et al. (2019) and Zhao et al. (2020) showed
416 that the trends are relatively insensitive to the specific beginning and ending time of the data as
417 compared to the data length. Since the data length used in this study spans approximately two solar
418 cycles, the derived trends are reliable in statistical sense. In the following discussions, the reliability
419 of trends will also be determined by comparing them with the systematic trend uncertainty.

420 **4.1 The reliability of trends in the MLT region at latitudes lower than 50°N/S**

421 To facilitate a comparison with previously reported the annual and global-mean trends in the
422 MLT region, we present the mean trends of the corrected mean temperature at 50°S–50°N and at
423 55–80°S or 55–80°N of the six YCs (Fig. 6). The mean trends at 50°S–50°N of each YC are cooling
424 with magnitudes of ~ 0.5 – 1 K/decade at 10 – 10^{-3} hPa. The exception is the warming trend of 0.2
425 K/decade around 10^{-2} hPa in YC1 and of 0.1 K/decade around 4×10^{-3} hPa in YC3. Above 5×10^{-3}
426 hPa, the cooling trends increase sharply with altitude and reach to ~ 2 K/decade in YC5 and to ~ 3
427 K/decade in YC2 at 10^{-4} hPa. Compared to the situation in YC2 and YC5, the cooling trends
428 increase more sharply with altitude in YC3 and YC6. Their magnitudes change nearly identically
429 and are from ~ 0.5 K/decade at 2×10^{-3} hPa to ≥ 5 K/decade at 10^{-4} hPa. When the mean trends at

430 50°S–50°N across all-YC are further averaged, we obtain an annual mean trend (blue line in Fig.
431 6a). The annual mean trend is cooling with magnitudes of $\sim 0.5\text{--}0.8$ K/decade and vary with altitude
432 slightly at $10\text{--}5\times 10^{-4}$ hPa.

433 The altitude variation and the magnitude of the annual mean trend are similar to the previous
434 results (Garcia et al., 2019; Mlynczak et al., 2022; Zhao et al., 2021). Figure 3 of Garcia et al.
435 (2019) revealed that the global mean (52°S–52°N) SABER temperature trends are cooling with
436 magnitudes of $\sim 0.5\text{--}0.9$ K/decade at $10\text{--}5\times 10^{-4}$ hPa during 2002–2018. These magnitudes are
437 slightly smaller than those derived from WACCM. Table 1 of Mlynczak et al. (2022) demonstrated
438 that the global mean (55°S–55°N) SABER temperature also display cooling trends with magnitudes
439 of $\sim 0.51\text{--}0.63$ K/decade at $1\text{--}10^{-3}$ hPa. Similarly, Fig. 4 of Zhao et al. (2021) revealed that the
440 global mean (50°S–50°N) SABER temperature trends are cooling with magnitudes of $\sim 0.5\text{--}0.9$
441 K/decade at 30–105 km. At 10^{-4} hPa, the extreme cooling trend of 2.6 K/decade in Table 1 of
442 Mlynczak et al. (2022) is slightly smaller than the 2.8 K/decade derived here but within 2 times of
443 the standard deviation (blue line in Fig. 6a). Further examining the trends across the six YCs (Figs.
444 4 and 6a), it becomes evident that the extreme cooling trend is mainly attributed to the middle
445 latitudes of summer hemisphere (i.e., YC3 and YC6) and partially from other months. As suggested
446 by Mlynczak et al. (2022), the extreme cooling trend at 10^{-4} hPa is due to a decrease in solar
447 irradiance that is not captured by the $F_{10.7}$ index.

448 We note that these trends are derived from the SABER temperature. The systematic error of
449 SABER temperature influences the credibility of these derived trends. According to the rigorous
450 analysis of the systematic error, the trends derived here are reliable only if their magnitudes are
451 larger than the systematic trend uncertainty. The annual and global-mean trends are cooling with
452 magnitudes of 2–4 K/decade around 10^{-4} hPa are unreliable. Because these values are in the range
453 of the systematic trend uncertainty of 22.7 K/decade at 6.3×10^{-5} hPa and 4.5 K/decade at 2.8×10^{-4}
454 hPa. At pressure levels lower than 10^{-3} hPa, the annual and global-mean trends are cooling with
455 magnitudes of $\sim 0.5\text{--}1$ K/decade are unreliable. Because these values are in the range of the
456 systematic trend uncertainty of 3.6 K/decade around 10^{-3} hPa and 1.3 K/decade below 6.6×10^{-3} hPa.

457 These detailed comparisons showed that the trends at pressure levels reported by Garcia et al.
458 (2019) and Mlynczak et al. (2022) support the altitude variations and magnitudes of the trends
459 derived here directly. Although the trends reported by Zhao et al. (2021) are in geometric height,
460 their altitude variations and magnitudes agree with the trends derived here, too. However, these
461 trends are unreliable since their magnitudes are in the range of the systematic trend uncertainties.
462 We note that the method of binning SABER samplings based on YC provides an opportunity to
463 study the trends at latitudes higher than 50°N/S in certain months.

464

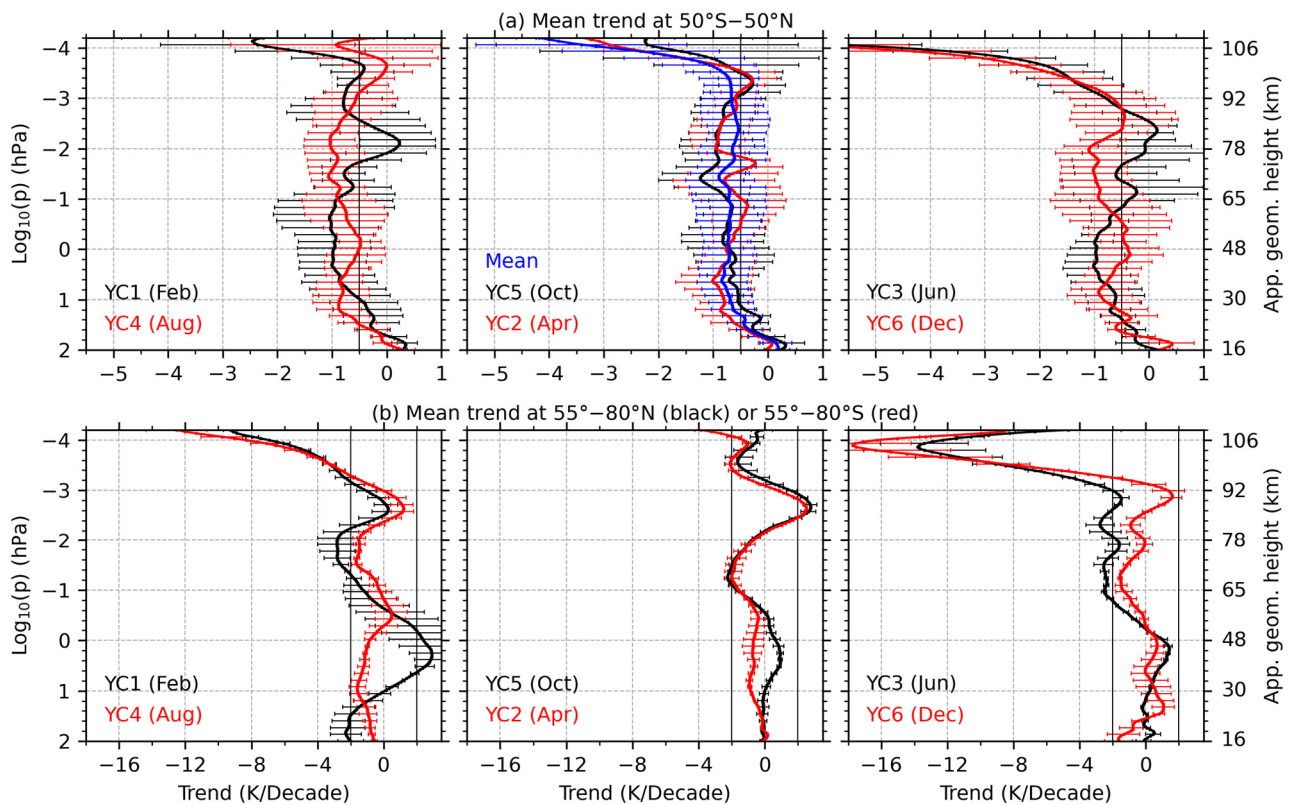


Figure 6. Mean trends of the corrected mean temperature at 50°S–50°N (a) and at 55–80°S (red line in b) or 55–80°N (black line in b) of the six YCs. The annual mean trend is calculated by averaging the trends of the six YCs at 50°S–50°N and is shown a blue line in the middle panel of (a). The error bars indicate standard errors of the averaged data.

465

466 **4.2 The reliability of trends in the MLT region at latitudes higher than 50°N/S**

467 At latitudes higher than 50°N/S, the altitude variations of the mean trends of the six YCs (Fig.
 468 6b) are seasonal symmetric approximately above 1 hPa. The magnitudes of trends are mainly in the
 469 range of -2–2 K/decade below the height of 10^{-3} hPa. These trends are larger than the systematic
 470 trend uncertainties of 1.3 K/decade and thus are reliable below 6.6×10^{-3} hPa. However, these trends
 471 are in the range of the systematic trend uncertainties of 3.6 K/decade and thus are unreliable around
 472 10^{-3} hPa. An interesting feature is the warming trends of 1–2.5 K/decade at 10^{-2} – 10^{-3} hPa in April,
 473 August, October, and December. The altitudes of peaks of the warming trends vary from 4×10^{-3} hPa
 474 to 10^{-3} hPa in different months. Focusing on the latitude band of 64–70°N in June and 64–70°S in
 475 December, Bailey et al. (2021) merged the temperature data from HALO and SABER (total length
 476 of 29 years) and HALOE and SOFIE (total length of 22 years). Their analysis revealed warming
 477 trends of 1–2 K/decade near 5×10^{-3} hPa (~ 85 km) at 64–70°N in June and 64–70°S in December, as
 478 illustrated in Fig. 7 of their paper. The results simulated by WACCM-X showed significant warming
 479 trends at ~ 80 – 95 km at latitudes higher than 45°S from November to February and close to zero or
 480 warming trends at latitudes higher than 45°N from June to July (Qian et al., 2019). The warming

481 trends in December derived here coincides with those reported by Bailey et al. (2021) and Qian et
 482 al. (2019). The weak warming trend at 2×10^{-3} hPa in June coincides with those in Qian et al. (2021)
 483 but is much smaller than the 1–2 K/decade reported by Bailey et al. (2021). In April and October,
 484 the warming trends are hemispheric symmetric at 10^{-2} – 10^{-3} hPa and reach peak of ≥ 2 K/decade at
 485 3×10^{-3} hPa. It should be noted that, the warming trends of 1–2.5 K/decade at 10^{-2} – 10^{-3} hPa are in
 486 the range of the systematic trend uncertainties of 1.3 K/decade at 6.6×10^{-3} hPa and of 3.6 K/decade
 487 around 10^{-3} hPa. Thus they are unreliable in the sense of systematic trend uncertainty. Above 10^{-3}
 488 hPa, the trends transit from warming to cooling.

489 We can see the extreme cooling trends of ≥ 6 K/decade above $\sim 10^{-3}$ hPa and in YC3 and YC6
 490 also in YC1 and YC4 but around 10^{-4} hPa. Due to the systematic trend uncertainty, these trends are
 491 reliable around 10^{-3} hPa but unreliable around 10^{-4} hPa. These cooling trends are comparable with
 492 the global average mesosphere temperature of 6.8–8.4 K/decade derived by Mlynczak et al. (2022)
 493 after doubling of CO₂ in the MLT region. However, it takes decades to doubled CO₂. Thus, a purely
 494 radiative effect due to the increasing CO₂ cannot support the extrem cooling trends derived here.
 495 Mlynczak et al. (2022) proposed that the F10.7 is not a suitable proxy to indicate effects of the solar
 496 radiations on the lower thermosphere. But the solar irradiance in the Schumann–Runge band (175–
 497 200 nm) might be responsible for the colder trend. Even so, the extreme cooling trends of ~ 10
 498 K/decade are still larger than those reported by Mlynczak et al. (2022). Other possible reasons for
 499 the extreme cooling trends in the high latitude MLT region can be attributed to the dynamical
 500 feedback in the polar MLT region.

501 Besides the purely radiative effect on the cooling trends in the MLT region (i.e., Garcia et al.,
 502 2019, Mlynczak et al., 2022), the dynamical feedback might be another cause of the cooling trends.
 503 Based on the simplified transformed Eulerian mean (TEM) thermodynamic equation, the
 504 temperature change (ΔT) caused by dynamics can be written as (Eq. 3 and 4 of Yu et al. (2023)),

$$505 \quad \Delta T = -\alpha^{-1} \left(w^* S + v^* \frac{\partial \bar{T}}{a \partial \varphi} \right). \quad (4)$$

506 Here, α is the Newtonian cooling coefficient. w^* and v^* are the residual vertical and meridional
 507 velocity, respectively. S and \bar{T} are the static stability and zonal mean temperature, respectively. a
 508 and φ are the Earth’s radius and latitude, respectively. From Eq. (4), we propose that the extreme
 509 cooling trends at high latitudes of the summer hemispheres (YC3 and YC6) might be resulted from
 510 the changing summer-to-winter circulation and gravity wave forcing in the MLT region. The
 511 circulation is upwelling (positive w^*) in the summer hemisphere and causes a cold summer
 512 mesosphere through adiabatic cooling. Conversely, in the winter hemisphere, the circulation is
 513 downwelling (negative w^*), leading to a warm winter mesosphere through adiabatic warming
 514 (Garcia and Solomon, 1985). A necessary condition for the extreme cooling trends at summer high

515 latitudes is the stronger upwelling and thus the increasing gravity wave body force in the summer
516 hemispheres. Previous studies showed that the potential energy of gravity waves (GWPE) in the
517 MLT region exhibited significant positive trends at southern high latitudes in January and at
518 northern high latitudes in July (Fig. 5 of Liu et al., 2017). The positive trends of GWPE might
519 enhance the strength of upwelling and thus result in the extreme cooling trends at high latitudes of
520 summer hemispheres. It should be noted that the dynamical feedback in the MLT region is only
521 analyzed qualitatively, the quantitative analysis should be performed through model simulations.
522 Such that one can elucidate the physics behind the strong cooling trend in the polar MLT region.

523

524 4.3 The reliability of the mesopause trends

525 The trends of \bar{T}_{msp} derived in this study are significant and mainly negative at 50°S–50°N
526 across most YCs. The averaged trend of \bar{T}_{msp} of the six YCs is -0.64 ± 0.22 K/decade over 50°S–
527 50°N. When the average is performed over 80°S–80°N, the trend of \bar{T}_{msp} of the six YCs is -
528 1.03 ± 0.40 K/decade. The cooling trend of \bar{T}_{msp} derived here coincides also with the -0.5 ± 0.21
529 K/decade in the mesosphere (Garcia et al., 2019) within only 50°S–50°N. Compared to the trend
530 derived from sodium lidar observations during nighttime only around 40°N, the trends of \bar{T}_{msp} from
531 SABER are about -0.1, 0.0, -0.2, -0.8, 0.6, -1.9 K/decade in the six YCs and have annual mean of -
532 0.4 K/decade. This is less than the significant cooling trend of 2.3–2.5 K/decade during 1990–2018
533 but is consistent with the insignificant cooling trend of 0.2–1 K/decade during 2000–2018 (Yuan et
534 al., 2019). The comparisons of \bar{T}_{msp} between our results and those from satellite, ground-based
535 observations exhibit general consistencies in the sense of annual mean or global-mean. However,
536 the z_{msp} is mainly above 95 km (6.5×10^{-4} hPa), where the systematic trend uncertainties are larger
537 than 3.8 K/decade and are larger than the trends of \bar{T}_{msp} . Thus, the trends of \bar{T}_{msp} derived here are
538 mainly unreliable in the sense of rigorous systematic error analysis.

539 A notable feature is the warming trends of \bar{T}_{msp} with magnitudes of 0–2 K/decade at latitudes
540 higher than 40°S in YC6. This warming trend is insignificant under 95% confidence level. If we
541 change the temporal interval from 2002–2023 to 2002–2019, the trends of \bar{T}_{msp} are cooling with
542 magnitudes of 1–2 K/decade. Here we note that the year 2020 is just after the time when the
543 SABER temperature data was revised (version 2.08, since 15 December 2019) (Mlynczak et al.,
544 2023). In this work, we use the SABER temperature data of versions 2.07 (before 15 December
545 2019) and 2.08 (after 15 December 2019). According to Mlynczak et al. (2023), the new released
546 data are free from the algorithm instability. On the other hand, there is no significant difference in
547 the counterpart of YC3. A recent study by Yu et al. (2023) showed that the Hunga Tonga Hunga-
548 Ha'apai (HTHH) volcanic eruption on 15 January 2022 induced temperature anomalies of ± 10 K

549 globally in the stratosphere and mesosphere in August. The anomalies disappeared after September
550 2022. This indicates that the volcanic eruption may influence the mesosphere temperature through
551 circulations and waves. From the mesopause temperature of YC6 shown in Fig. 3, we see that the
552 warmer mesopause occurred after 2020 before the HTHH volcanic eruption. Thus, the largest
553 difference in YC6 may not be caused by the algorithm instability or the HTHH volcanic eruption but
554 a realistic result. As shown in Figs. 2(d) and 5(b) and reported by Wang et al. (2022), the annual
555 variability of z_{msp} is ~ 5 km at the southern high latitudes (YC6) but is relative stable at the northern
556 high latitudes (YC3). The large annual variability of z_{msp} induces a large variability of \bar{T}_{msp}
557 (indicated by large standard deviations in the right panel of Fig. 5b). This in turn contributes to the
558 large variability of the trends of \bar{T}_{msp} at southern high latitudes. Another possible reason is that the
559 warming trends of 0–2 K/decade are unreliable due to the large systematic trend uncertainties in this
560 height range.

561 **5 Summary**

562 Using the temperature profiles measured by the SABER instrument throughout the period of
563 2002–2023 (about two solar cycles) and binning them based on yaw cycles (YCs), we get
564 continuous data with good LT coverage within the range of 50°S–80°N or 80°S–50°N. Then we can
565 obtain an accurate mean temperature excluding atmospheric waves. The temporal span of each YC
566 drifted forward about one month from 2002 to 2023, aliasing the seasonal change in temperature
567 into long-term trends. This season change is removed by using the climatological temperature of
568 MSISE2.0. The remaining temperature is regarded as the corrected mean temperature (\bar{T}_{bcrt}^{year}) of
569 each YC. Then the mesopause temperature (\bar{T}_{msp}) and height (\bar{z}_{msp}) are calculated from \bar{T}_{bcrt}^{year} .
570 Such that the trends of the mean temperature and the mesopause structure can be studied in each YC
571 at high latitudes using MLR. The main results are summarized as below:

572 The cooling trends are significant in the MLT region and coincide well with previous results at
573 50°S–50°N. At latitudes higher than 55°N, the new findings are that the cooling trends have
574 magnitudes of ≥ 2 K/decade at northern high latitudes in February, April, and June and at southern
575 high latitudes in August, October, and December. There are also extreme cooling trends of ≥ 6
576 K/decade in the lower thermosphere at the northern high latitude in February and June and at the
577 southern high latitudes in August and December. Both the cooling and extreme cooling trends are
578 hemispheric and seasonal symmetric. It should be noted that the annual and global-mean trends are
579 unreliable in the sense of rigorous systematic error analysis. The trend of each YC are reliable
580 only below 6.6×10^{-3} hPa. The extreme cooling trends of ≥ 6 K/decade in YC3 and YC6 are reliable
581 above $\sim 10^{-3}$ hPa in the sense of rigorous systematic error analysis.

582 Besides the general cooling trends, there are also warming trends of 1–2.5 K/decade at 10^{-2} – 10^{-1}

583 ³ hPa and at latitudes higher than 55°N in October and December and at latitudes higher than 55°S
584 in April and August. The peaks of the warming trends vary from 4×10^{-3} hPa to 10^{-3} hPa in different
585 months. The warming trend in December coincides with previous observational and simulation
586 results. However, these warming trends are in the range of the systematic trend uncertainties.

587 The mean $\bar{T}_{msp}(z_{msp})$ in the northern summer polar region is colder (lower) than that in the
588 southern counterpart by a value of $\sim 5\text{--}11$ K (~ 1 km) over the past 22 years. Although the trends of
589 \bar{T}_{msp} are highly dependent on latitudes and months, they are negative at most latitudes and have
590 larger magnitudes at higher latitudes. The trends of \bar{T}_{msp} at the southern high latitudes in December
591 are highly dependent on the data length. The trends of \bar{T}_{msp} change from warming of 0–2 K/decade
592 during 2002–2023 to cooling of 1–2 K/decade during 2002–2019. The significant dependence of the
593 trends of \bar{T}_{msp} on the data length might be caused by the large annual variability of z_{msp} at the
594 southern high latitudes in December. However, the trends of \bar{T}_{msp} derived here are mainly
595 unreliable in the sense of rigorous systematic analysis.

596 The trends of the mean temperature in the MLT region and mesopause are revealed from
597 continuous observations of the SABER instrument over the past 22 years. The data length is long
598 enough to determine reliable trends. Our results provide an observational proof that the extreme
599 cooling trends at high latitudes are more sensitive to the changing dynamics associated with climate
600 change and should be paid more attentions in future observational and model studies. Another
601 important issue is the systematic error in SABER operational processing. The trends derived here
602 are mostly unreliable in the sense of rigorous systematic error analysis. The only reliable trends are
603 the extreme cooling trends of ≥ 6 K/decade in YC3 and YC6.

604

605 **Author contributions**

606 XL analyzed the data and prepared the paper with assistance from all co-authors. JX and JY
607 design the study. All authors reviewed and commented on the paper.

608 **Data Availability Statement**

609 All SABER data can be accessed from Space Physics Data Facility, Goddard Space Flight
610 Center (<https://spdf.gsfc.nasa.gov/pub/data/timed/saber/> (last access: January 2024; Mlynczak et al.,
611 2023). The $F_{10.7}$ data were obtained from <https://spdf.gsfc.nasa.gov/pub/data/omni/> (last access:
612 January 2024; Tapping, 2013). The ENSO data were obtained from
613 <https://www.psl.noaa.gov/enso/mei/> (last access: January 2024; Zhang et al., 2019; Wolter and
614 Timlin, 2011)

615 **Competing interests**

616 The authors declare that they have no conflict of interest.

617 **Acknowledgments**

618 This work was supported by the National Natural Science Foundation of China (41874182,
619 42174196), the Project of Stable Support for Youth Team in Basic Research Field, CAS (YSBR-
620 018), the Informatization Plan of Chinese Academy of Sciences (CAS-WX2021PY-0101), and the
621 Open Research Project of Large Research Infrastructures of CAS "Study on the interaction between
622 low/mid-latitude atmosphere and ionosphere based on the Chinese Meridian Project". This work
623 was also supported in part by the Specialized Research Fund and the Open Research Program of the
624 State Key Laboratory of Space Weather. We are very grateful for the helpful comments by Jan
625 Laštovička, Martin Mlynczak, Tao Yuan, and Ana G. Elias.

626 **References**

- 627 Bailey, S. M., Thurairajah, B., Hervig, M. E., Siskind, D. E., Russell, J. M., and Gordley, L. L.: Trends in the polar
628 summer mesosphere temperature and pressure altitude from satellite observations, *J. Atmos. Solar-Terrestrial*
629 *Phys.*, 220, 105650, <https://doi.org/10.1016/j.jastp.2021.105650>, 2021.
- 630 Beig, G., Keckhut, P., Lowe, R. P., Roble, R. G., Mlynczak, M. G., Scheer, J., Fomichev, V. I., Offermann, D., French,
631 W. J. R., Shepherd, M. G., Semenov, A. I., Remsberg, E. E., She, C. Y., Lübken, F. J., Bremer, J., Clemesha, B. R.,
632 Stegman, J., Sigernes, F., and Fadnavis, S.: Review of mesospheric temperature trends, *Rev. Geophys.*, 41,
633 <https://doi.org/10.1029/2002RG000121>, 2003.
- 634 Beig, G., Scheer, J., Mlynczak, M. G., and Keckhut, P.: Overview of the temperature response in the mesosphere and
635 lower thermosphere to solar activity, *Rev. Geophys.*, 46, <https://doi.org/10.1029/2007RG000236>, 2008.
- 636 Dalin, P., Perminov, V., Pertsev, N., and Romejko, V.: Updated Long-Term Trends in Mesopause Temperature,
637 Airglow Emissions, and Noctilucent Clouds, *J. Geophys. Res. Atmos.*, 125, 1–19,
638 <https://doi.org/10.1029/2019JD030814>, 2020.
- 639 Das, U.: Spatial variability in long-term temperature trends in the middle atmosphere from SABER/TIMED
640 observations, *Adv. Sp. Res.*, 68, 2890–2903, <https://doi.org/10.1016/j.asr.2021.05.014>, 2021.
- 641 Dawkins, E. C. M., Feofilov, A., Rezac, L., Kutepov, A. A., Janches, D., Höffner, J., Chu, X., Lu, X., Mlynczak, M. G.,
642 and Russell, J.: Validation of SABER v2.0 operational temperature data with ground-based lidars in the
643 mesosphere-lower thermosphere region (75–105 km), *J. Geophys. Res. Atmos.*, 123, 9916–9934,
644 <https://doi.org/10.1029/2018JD028742>, 2018.
- 645 Domeisen, D. I. V., Garfinkel, C. I., and Butler, A. H.: The teleconnection of El Niño Southern Oscillation to the
646 stratosphere, *Rev. Geophys.*, 57, 5–47, <https://doi.org/10.1029/2018RG000596>, 2019.
- 647 Dunkerton, T.: On the mean meridional mass motions of the stratosphere and mesosphere, *J. Atmos. Sci.*, 35, 2325–
648 2333, [https://doi.org/10.1175/1520-0469\(1978\)035<2325:OTMMMM>2.0.CO;2](https://doi.org/10.1175/1520-0469(1978)035<2325:OTMMMM>2.0.CO;2), 1978.
- 649 Emmert, J. T., Drob, D. P., Picone, J. M., Siskind, D. E., Jones, M., Mlynczak, M. G., Bernath, P. F., Chu, X.,
650 Doornbos, E., Funke, B., Goncharenko, L. P., Hervig, M. E., Schwartz, M. J., Sheese, P. E., Vargas, F., Williams,
651 B. P., and Yuan, T.: NRLMSIS 2.0: a whole-atmosphere empirical model of temperature and neutral species
652 densities, *Earth Sp. Sci.*, 8, <https://doi.org/10.1029/2020EA001321>, 2021.
- 653 Forbes, J. M., Zhang, X., and Marsh, D. R.: Solar cycle dependence of middle atmosphere temperatures, *J. Geophys.*
654 *Res. Atmos.*, 119, 9615–9625, <https://doi.org/10.1002/2014JD021484>, 2014.
- 655 French, W. J. R., Mulligan, F. J., and Klekociuk, A. R.: Analysis of 24 years of mesopause region OH rotational

656 temperature observations at Davis, Antarctica – Part 1: long-term trends, *Atmos. Chem. Phys.*, 20, 6379–6394,
657 <https://doi.org/10.5194/acp-20-6379-2020>, 2020.

658 Gan, Q., Du, J., Fomichev, V. I., Ward, W. E., Beagley, S. R., Zhang, S., and Yue, J.: Temperature responses to the 11
659 year solar cycle in the mesosphere from the 31 year (1979–2010) extended Canadian Middle Atmosphere Model
660 simulations and a comparison with the 14 year (2002–2015) TIMED/SABER observations, *J. Geophys. Res. Sp.*
661 *Phys.*, 122, 4801–4818, <https://doi.org/10.1002/2016JA023564>, 2017.

662 Garcia, R. R. and Solomon, S.: The effect of breaking gravity waves on the dynamics and chemical composition of the
663 mesosphere and lower thermosphere., *J. Geophys. Res.*, 90, 3850–3868, <https://doi.org/10.1029/JD090iD02p03850>,
664 1985.

665 Garcia, R. R., Yue, J., and Russell, J. M.: Middle atmosphere temperature trends in the twentieth and twenty-First
666 centuries simulated with the Whole Atmosphere Community Climate Model (WACCM), *J. Geophys. Res. Sp.*
667 *Phys.*, 124, 7984–7993, <https://doi.org/10.1029/2019JA026909>, 2019.

668 Kutner, M., Neter, C. N. J., and Li, W.: *Applied linear statistical models*, 5th ed., McGraw-Hill Irwin, Boston, 1396 pp.,
669 2005.

670 Laštovička, J.: Global pattern of trends in the upper atmosphere and ionosphere: Recent progress, *J. Atmos. Solar-*
671 *Terrestrial Phys.*, 71, 1514–1528, <https://doi.org/10.1016/j.jastp.2009.01.010>, 2009.

672 Laštovička, J.: Progress in investigating long-term trends in the mesosphere, thermosphere, and ionosphere, *Atmos.*
673 *Chem. Phys.*, 23, 5783–5800, <https://doi.org/10.5194/acp-23-5783-2023>, 2023.

674 Laštovička, J. and Jelínek, Š.: Problems in calculating long-term trends in the upper atmosphere, *J. Atmos. Solar-*
675 *Terrestrial Phys.*, 189, 80–86, <https://doi.org/10.1016/j.jastp.2019.04.011>, 2019.

676 Laštovička, J., Akmaev, R. A., Beig, G., Bremer, J., and Emmert, J. T.: Global Change in the Upper Atmosphere,
677 *Science (80-.)*, 314, 1253–1254, <https://doi.org/10.1126/science.1135134>, 2006.

678 Li, T., Calvo, N., Yue, J., Dou, X., Russell, J. M., Mlynczak, M. G., She, C. Y., and Xue, X.: Influence of El Niño-
679 Southern oscillation in the mesosphere, *Geophys. Res. Lett.*, 40, 3292–3296, <https://doi.org/10.1002/grl.50598>,
680 2013.

681 Li, T., Calvo, N., Yue, J., Russell, J. M., Smith, A. K., Mlynczak, M. G., Chandran, A., Dou, X., and Liu, A. Z.:
682 Southern Hemisphere summer mesopause responses to El Niño-Southern Oscillation, *J. Clim.*, 29, 6319–6328,
683 <https://doi.org/10.1175/JCLI-D-15-0816.1>, 2016.

684 Li, T., Yue, J., Russell, J. M., and Zhang, X.: Long-term trend and solar cycle in the middle atmosphere temperature
685 revealed from merged HALOE and SABER datasets, *J. Atmos. Solar-Terrestrial Phys.*, 212, 105506,
686 <https://doi.org/10.1016/j.jastp.2020.105506>, 2021.

687 Liu, X., Yue, J., Xu, J., Garcia, R. R., Russell, J. M., Mlynczak, M., Wu, D. L., and Nakamura, T.: Variations of global
688 gravity waves derived from 14 years of SABER temperature observations, *J. Geophys. Res. Atmos.*, 122, 6231–
689 6249, <https://doi.org/10.1002/2017JD026604>, 2017.

690 Lübken, F. J., Berger, U., and Baumgarten, G.: On the anthropogenic impact on long-term evolution of noctilucent
691 clouds, *Geophys. Res. Lett.*, 45, 6681–6689, <https://doi.org/10.1029/2018GL077719>, 2018.

692 Lübken, F. J., Baumgarten, G., and Berger, U.: Long term trends of mesospheric ice layers: A model study, *J. Atmos.*
693 *Solar-Terrestrial Phys.*, 214, 105378, <https://doi.org/10.1016/j.jastp.2020.105378>, 2021.

694 Mlynczak, M. G., Daniels, T., Hunt, L. A., Yue, J., Marshall, B. T., Russell, J. M., Remsberg, E. E., Tansock, J., Esplin,
695 R., Jensen, M., Shumway, A., Gordley, L., and Yee, J. H.: Radiometric stability of the SABER instrument, *Earth*
696 *Sp. Sci.*, 7, 1–8, <https://doi.org/10.1029/2019EA001011>, 2020.

697 Mlynczak, M. G., Hunt, L. A., Garcia, R. R., Harvey, V. L., Marshall, B. T., Yue, J., Mertens, C. J., and Russell, J. M.:
698 Cooling and contraction of the mesosphere and lower thermosphere from 2002 to 2021, *J. Geophys. Res. Atmos.*,
699 127, 1–17, <https://doi.org/10.1029/2022JD036767>, 2022.

700 Mlynczak, M. G., Marshall, B. T., Garcia, R. R., Hunt, L., Yue, J., Harvey, V. L., Lopez-Puertas, M., Mertens, C., and
701 Russell, J.: Algorithm stability and the long-term geospace data record from TIMED/SABER, *Geophys. Res. Lett.*,

702 50, 1–7, <https://doi.org/10.1029/2022GL102398>, 2023.

703 Qian, L., Burns, A., and Yue, J.: Evidence of the lower thermospheric winter-to-summer circulation from SABER CO₂

704 observations, *Geophys. Res. Lett.*, 44, 10,100–10,107, <https://doi.org/10.1002/2017GL075643>, 2017.

705 Qian, L., Jacobi, C., and McInerney, J.: Trends and solar irradiance effects in the mesosphere, *J. Geophys. Res. Sp.*

706 *Phys.*, 124, 1343–1360, <https://doi.org/10.1029/2018JA026367>, 2019.

707 Ramesh, K., Smith, A. K., Garcia, R. R., Marsh, D. R., Sridharan, S., and Kishore Kumar, K.: Long-term variability and

708 tendencies in middle atmosphere temperature and zonal wind from WACCM6 simulations during 1850–2014, *J.*

709 *Geophys. Res. Atmos.*, 125, <https://doi.org/10.1029/2020JD033579>, 2020.

710 Randel, W. J., Garcia, R. R., Calvo, N., and Marsh, D.: ENSO influence on zonal mean temperature and ozone in the

711 tropical lower stratosphere, *Geophys. Res. Lett.*, 36, n/a-n/a, <https://doi.org/10.1029/2009GL039343>, 2009.

712 Remsberg, E. E., Marshall, B. T., Garcia-Comas, M., Krueger, D., Lingenfelter, G. S., Martin-Torres, J., Mlynczak, M.

713 G., Russell, J. M., Smith, A. K., Zhao, Y., Brown, C., Gordley, L. L., Lopez-Gonzalez, M. J., Lopez-Puertas, M.,

714 She, C. Y., Taylor, M. J., and Thompson, R. E.: Assessment of the quality of the version 1.07 temperature-versus-

715 pressure profiles of the middle atmosphere from TIMED/SABER, *J. Geophys. Res. Atmos.*, 113, 1–27,

716 <https://doi.org/10.1029/2008JD010013>, 2008.

717 Rezac, L., Kutepov, A., Russell, J. M., Feofilov, A. G., Yue, J., and Goldberg, R. A.: Simultaneous retrieval of T(p) and

718 CO₂ VMR from two-channel non-LTE limb radiances and application to daytime SABER/TIMED measurements,

719 *J. Atmos. Solar-Terrestrial Phys.*, 130–131, 23–42, <https://doi.org/10.1016/j.jastp.2015.05.004>, 2015.

720 Russell, J. M., Bailey, S. M., Gordley, L. L., Rusch, D. W., Horányi, M., Hervig, M. E., Thomas, G. E., Randall, C. E.,

721 Siskind, D. E., Stevens, M. H., Summers, M. E., Taylor, M. J., Englert, C. R., Espy, P. J., McClintock, W. E., and

722 Merkel, A. W.: The Aeronomy of Ice in the Mesosphere (AIM) mission: Overview and early science results, *J.*

723 *Atmos. Solar-Terrestrial Phys.*, 71, 289–299, <https://doi.org/10.1016/j.jastp.2008.08.011>, 2009.

724 She, C. Y., Berger, U., Yan, Z., Yuan, T., Lübken, F. -J., Krueger, D. A., and Hu, X.: Solar response and long-term

725 trend of midlatitude mesopause region temperature based on 28 years (1990–2017) of Na lidar observations, *J.*

726 *Geophys. Res. Sp. Phys.*, 124, 7140–7156, <https://doi.org/10.1029/2019JA026759>, 2019.

727 Tapping, K. F.: The 10.7 cm solar radio flux (F 10.7), *Sp. Weather*, 11, 394–406, <https://doi.org/10.1002/swe.20064>,

728 2013.

729 Venkat Ratnam, M., Akhil Raj, S. T., and Qian, L.: Long-term trends in the low-latitude middle atmosphere

730 temperature and winds: observations and WACCM-X model simulations, *J. Geophys. Res. Sp. Phys.*, 124, 7320–

731 7331, <https://doi.org/10.1029/2019JA026928>, 2019.

732 Wang, N., Qian, L., Yue, J., Wang, W., Mlynczak, M. G., and Russell, J. M.: Climatology of mesosphere and lower

733 thermosphere residual circulations and mesopause height derived from SABER observations, *J. Geophys. Res.*

734 *Atmos.*, 127, 1–14, <https://doi.org/10.1029/2021JD035666>, 2022.

735 Xu, J., Liu, H.-L., Yuan, W., Smith, A. K., Roble, R. G., Mertens, C. J., Russell, J. M., and Mlynczak, M. G.:

736 Mesopause structure from Thermosphere, Ionosphere, Mesosphere, Energetics, and Dynamics (TIMED)/Sounding

737 of the Atmosphere Using Broadband Emission Radiometry (SABER) observations, *J. Geophys. Res.*, 112, D09102,

738 <https://doi.org/10.1029/2006JD007711>, 2007.

739 Yu, W., Garcia, R., Yue, J., Smith, A., Wang, X., Randel, W., Qiao, Z., Zhu, Y., Harvey, V. L., Tilmes, S., and

740 Mlynczak, M.: Mesospheric temperature and circulation response to the Hunga Tonga-Hunga-Ha’apai volcanic

741 eruption, *J. Geophys. Res. Atmos.*, 128, 1–10, <https://doi.org/10.1029/2023JD039636>, 2023.

742 Yuan, T., Solomon, S. C., She, C. -Y., Krueger, D. A., and Liu, H. -L.: The long-term trends of nocturnal mesopause

743 temperature and altitude revealed by Na lidar observations between 1990 and 2018 at midlatitude, *J. Geophys. Res.*

744 *Atmos.*, 124, 5970–5980, <https://doi.org/10.1029/2018JD029828>, 2019.

745 Yue, J., Russell, J., Jian, Y., Rezac, L., Garcia, R., López-Puertas, M., and Mlynczak, M. G.: Increasing carbon dioxide

746 concentration in the upper atmosphere observed by SABER, *Geophys. Res. Lett.*, 42, 7194–7199,

747 <https://doi.org/10.1002/2015GL064696>, 2015.

748 Yue, J., Russell, J., Gan, Q., Wang, T., Rong, P., Garcia, R., and Mlynczak, M.: Increasing water vapor in the
749 stratosphere and mesosphere after 2002, *Geophys. Res. Lett.*, 46, 13452–13460,
750 <https://doi.org/10.1029/2019GL084973>, 2019a.

751 Yue, J., Li, T., Qian, L., Lastovicka, J., and Zhang, S.: Introduction to special issue on “Long-term changes and trends
752 in the middle and upper atmosphere,” *J. Geophys. Res. Sp. Phys.*, 124, 10360–10364,
753 <https://doi.org/10.1029/2019JA027462>, 2019b.

754 Zhang, S., Cnossen, I., Laštovička, J., Elias, A. G., Yue, X., Jacobi, C., Yue, J., Wang, W., Qian, L., and Goncharenko,
755 L.: Long-term geospace climate monitoring, *Front. Astron. Sp. Sci.*, 10, 1–5,
756 <https://doi.org/10.3389/fspas.2023.1139230>, 2023.

757 Zhao, X. R., Sheng, Z., Shi, H. Q., Weng, L. B., and Liao, Q. X.: Long-term trends and solar responses of the
758 mesopause temperatures observed by SABER during the 2002–2019 period, *J. Geophys. Res. Atmos.*, 125, 1–17,
759 <https://doi.org/10.1029/2020JD032418>, 2020.

760 Zhao, X. R., Sheng, Z., Shi, H. Q., Weng, L. B., and He, Y.: Middle atmosphere temperature changes derived from
761 SABER observations during 2002-2020, *J. Clim.*, 34, 1, <https://doi.org/10.1175/JCLI-D-20-1010.1>, 2021.

762